Structural optimization of 3D-printed patient-specific ceramic scaffolds for *in vivo* bone regeneration in load-bearing defects

Pablo Blázquez-Carmona [a,*], José Antonio Sanz-Herrera [a], Francisco Javier Martínez-Vázquez [b], Jaime Domínguez [a], Esther Reina-Romo [a]

[a] E.T.S.I, Universidad de Sevilla, Avenida Camino de los Descubrimientos s/n, 41092, Seville, Spain
[b] Escuela de Ingenierías Industriales, Universidad de Extremadura, Avda. de Elvas, s/n, 06006, Badajoz, Spain

ARTICLE INFO

ABSTRACT

Tissue engineering has recently gained popularity as an alternative to autografts to stimulate bone tissue regeneration through structures called scaffolds. Most of the *in vivo* experiments on long-bony defects use internally-stabilized generic scaffolds. Despite the wide variety of computational methods, a standardized protocol is required to optimize ceramic scaffolds for load-bearing bony defects stabilized with flexible fixations. An optimization problem was defined for applications to sheep metatarsus defects. It covers biological parameters (porosity, pore size, and the specific surface area) and mechanical constraints based on *in vivo* and *in vitro* results reported in the literature. The optimized parameters (59.30% of porosity, 5768.91 m^{-1} of specific surface area, and 360.80 μm of pore size) and the compressive strength of the selected structure were validated *in vitro* by means of tomographic images and compression tests of six 3D-printed samples. Divergences between the design and measured values of the optimized parameters, mainly due to manufacturing defects, are consistent with the previous studies. Using the mixed experimental-mathematical scaffold-design procedure described, they could be implanted *in vivo* with instrumented external fixators, therefore facilitating biomechanical monitoring of the regeneration process.

1. Introduction

Autograft is traditionally considered as the bony benchmark substitute for the treatment of skeletal defects. Nonetheless, its main drawback lies in the limited resource availability, especially for critical-size defects. Besides, patients usually report pain in the donor site, as well as long-term functional damage (Silber et al. (2003)). As an alternative, tissue engineering (TE) has rapidly emerged as a clinical research field focused on the replacement and healing of damaged bone tissue using porous scaffolds (Berthiaume et al. (2011)). These structures play the dual function of providing mechanical support and guiding the tissue formation, offering the necessary surface for cell adhesion and proliferation.

Among the materials commonly used are natural and synthetic polymers (Seal et al. (2001); Bressan et al. (2011)), metals (Boccaccio et al. (2016a)), or ceramics (Hulbert et al. (1970); Bohner and Baumgart (2004); Miranda et al. (2007); Bai et al. (2010); Dawson et al. (2018)).

Many technological platforms and manufacturing processes succeeded in combining these materials to fabricate bioconstructs for different TE applications, including coaxial bioprinting, wet spinning, melt electrospinning writing, or stereolithography (Rainer and Moroni). Focusing on bone TE, bioceramic materials (e.g., hydroxyapatite or calcium phosphate cement) have recently become more popular in clinical research due to their high biocompatibility, osteoconductivity, and their bioabsorbable properties (Hulbert et al. (1970); Bohner (2000); Sanz-Herrera et al. (2010); Feng et al. (2011); Pobloth et al. (2018); Pina et al. (2019)). These materials are generally compatible with additive manufacturing (AM) techniques (Chocholata et al. (2019)). The main advantage of AM lies in controlling the internal interconnected architecture and the pore size distribution to promote bone formation (Yang et al. (2002); Sachlos and Czernuszka (2003)). This property has improved the prototyping of scaffolds with a multitude of architectures: structures with periodic pores, CAD designs based on solid primitives, surface-based architectures, or even image-based designs (Giannitelli

---

et al. (2014a)). Their structural assembly by deposition can also build complex patient-specific outer shapes from tomographic data or other medical imaging techniques. Besides, recent studies have examined biological benefits when combining AM with other fabrication methods at the assembly, fabrication, or technique levels (Giannitelli et al. (2015)). Robocasting is the most common AM technique because of the high porosity levels achieved through continuous extrusion of highly concentrated powder slurries that largely retain their shape during assembly (Miranda et al. (2007, 2008); Eqtesadi et al. (2015)).

Several methods for optimizing medical structures for bone TE are reported in the literature. For instance, the studies of Boccaccio et al. (2016a,b) focused on shape optimization to control the mechanobiological stimulus for bone regeneration from topological parameters. Despite including constraints for mechanical parameters, the topology optimization algorithm of Dias et al. (2014) prioritized the maximization of permeability to guarantee cell diffusion. Uth et al. (2017) studied compressive mechanical strength and porosity by simplifying the topology problem to three factors: hydroxyapatite content, strand diameter, and strand spacing. Hollister et al. (2002) described an image-based optimization procedure based on creating scaffolds that, together with the regenerated tissue, match host tissue stiffness while meeting additional biological requirements. Sanz-Herrera et al. (2008, 2009, 2010) reported a multiscale mathematical approach to bone tissue regeneration using scaffolds. This technique provides macroscopic and bone distribution information on the scaffold microarchitecture. Despite the diversity of computational approaches, most of these studies were clinically applied without considering the mechanobiological particularities of each bone and animal model. Furthermore, they lack an *in vitro* validation that, simulating the specific mechanical boundary conditions to which the implant will be subjected *in vivo*, ensure its mechanical integrity until tissue regeneration. Proven standardized protocols, combining numerical design and experimental characterization, are required for the structural optimization of scaffolds applicable to specific critical-size load-bearing bony defects, but that are easily applicable to other bony models.

Most prior TE experimental research concentrates on assessing *in vitro* the mechanical strength of the scaffolds and their cell viability by cultivating mesenchymal stem cells (Mauney et al. (2005); Krieghoff et al. (2019)). Nevertheless, a considerable body of literature also focused on *in vivo* TE approaches through clinical interventions in several bony structures (Mauney et al. (2005); Feng et al. (2011); Cipitria et al. (2013); Lao et al. (2014); Dawson et al. (2018); Pobloth et al. (2018)). Rodent species are popular animal models among researchers due to their low price, availability, manageable size, and limited social concern (Gomes and Fernandes (2011); Li et al. (2015); El-Rashidy et al. (2017)). In particular, the calvariae bone is the most widely used defect model because of the large number of proven methodologies to monitor its regeneration progress (e.g., histological analysis or imaging techniques) and no fixation is needed for mechanical stabilization (Gomes and Fernandes (2011)). Despite the fixation requirement and the greater surgical complexity, cell proliferation has also been studied *in vivo* in bony models with structural, physiological and mechanical similarities to human limb bones, including dogs, pigs or sheep (Liu et al. (2010); Wang et al. (2010); Cipitria et al. (2013); Oh et al. (2015); McGovern et al. (2018); Pobloth et al. (2018)). Ovine animals stand out above the rest due to their comparable remodelling rates (den Boer et al. (1999)), promoting the extrapolation of the findings to human applications. Most of the *in vivo* studies on these long-bony models use generic scaffolds or do not detail the selection of their structure (den Boer et al. (1999); Liu et al. (2010); Wang et al. (2010); Cipitria et al. (2013); Dawson et al. (2018)).

In TE, internal fixations are popularly used to stabilize long-bony defects, such as intramedullary nails or bone plates (Liu et al. (2010); Wang et al. (2010); Cipitria et al. (2013); Histing et al. (2016)). Despite the numerous applications in distraction osteogenesis and fracture healing, few studies have used external fixators in TE applications to date (Oh et al. (2015); Pobloth et al. (2018)). Their greater flexibility, caused by the bending of the pins attached to the treated bone during surgery (Blázquez-Carmona et al. (2020b)), could be the reason why they have not been popularly implanted. Fixation stiffness should therefore be considered a critical factor in optimizing a load-bearing implant structure externally stabilized for *in vivo* experiments, especially in the early post-surgical stages. The advantages provided by these external fixations range from preventing interference with biological responses to the bony defects (Gugala et al. (2007); McGovern et al. (2018)) to the proven ease of instrumentation for the mechanical monitoring of the bone regeneration process (Duda et al. (1997); Mora-Macías et al. (2015a,b); Blázquez-Carmona et al. (2020a)). From the author's point of view, there are some potentially open questions to explore the applicability of these monitoring techniques to TE that justify the implantation of external fixations in this field.

This paper aims to define an optimization procedure for ceramic-based patient-specific scaffolds manufactured by AM technique for *in vivo* experiments in ovine long-bony models stabilized by external fixators and, therefore, with a certain tolerance for flexible fixations. The procedure is based on previous *in vivo* and *in vitro* experiments to define the objectives and constraints of several biological and mechanical parameters. The geometric parameters and failure criteria that compose the optimization problem are validated *in vitro* to ensure the *in vivo* implantability of the selected scaffold. The established experimental-mathematical approach is shown to be useful as a standard protocol for scaffold design in bone TE, especially for model parameters calibration and validation which are frequently missing in theoretical studies in this field.

2. Materials and methods

This section presents the methodology followed to optimize the structure of 3D-printed scaffolds for *in vivo* experiments in a right-back merino sheep metatarsus. A preliminary design of the patient-specific scaffold is shown in Fig. 1a. The size of the bony defect to be regenerated is set to 15 mm, corresponding to the length of the widest cross-section of the design. Two extra cantilevers, 2 mm long and with a smaller cross-section, are located at either end of the previous segment. Their primary function is to fit inside the bone marrow of both bony fragments and immobilize it during bone regeneration (Fig. 1a, marrow coupler). Furthermore, the defect will be stabilized using an external fixator with an axial stiffness (K_f) of 593 ± 21 N/mm and a length of 112.5 mm. This fixator has already been successfully implemented in previous *in vivo* studies of distraction osteogenesis (Blázquez-Carmona et al. (2020a,b, 2021)).

In the following subsections, the modifiable variables that define the potential geometric structures of the scaffold will be presented. Moreover, the biological and mechanical criteria involved in the optimization problem will be described, as well as the *in vitro* validation carried out by means of six 3D-printed scaffolds and a cadaveric sheep metatarsus. Table A.3 (appendix A) summarizes all parameters involved in this study, their definition, as well as their equation and value, if applicable.

2.1. Manufacturing and geometric variables

Robocasting is the selected 3D-printed technique to manufacture hydroxyapatite (HA) scaffolds. A concentration of commercial ceramic powder in distilled water is mixed with dispersing and gelling agents, resulting in a viscose robocasting ink with a content of 45 vol % for HA. Scaffolds are fabricated by the deposition of perpendicular layers of parallel rods in an oil bath to avoid any non-uniform drying during the manufacturing process (Miranda et al. (2008)), as shown in Fig. 1b. After a 24-h drying process at room temperature, scaffolds are heated at 400 °C for 1 h to remove organic components and finally sintered at 1300 °C for 2 h. The elastic modulus of the sintered material were measured on five rods for later computational use. Indentation tests
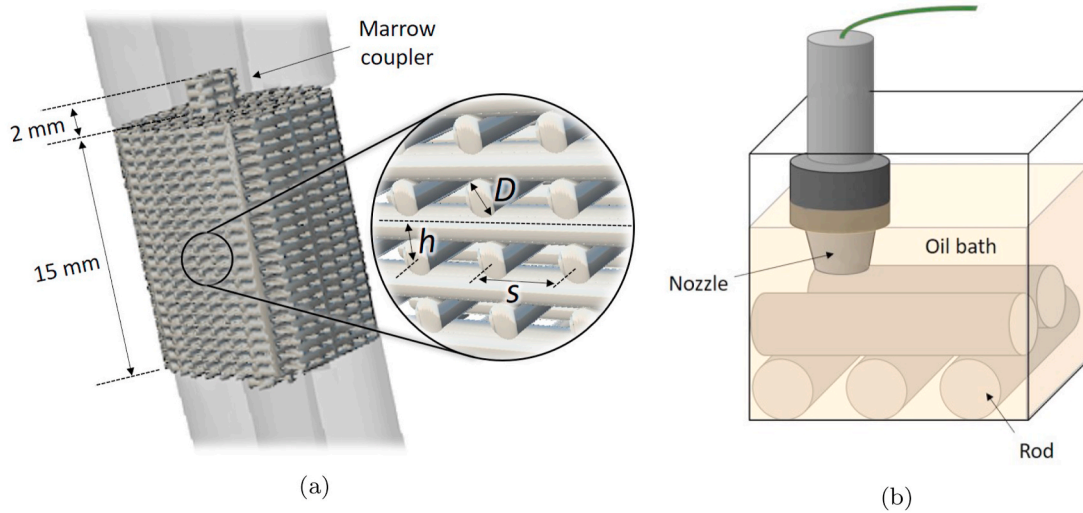
Fig. 1. (a) Preliminary design of scaffolds for the treatment of 15 mm bony defects. Two 2 mm couplers are included to fit inside the bone marrow at either end of the defect and immobilize the scaffold during the regeneration process. The implant structure after sintering is composed of rods with diameter *D*. The distance between rods in the same layer (from axis to axis) is defined by the variable *s*. The overlap between perpendicular layers is also controlled by *h*. (b) Diagram of the robocasting ceramic scaffold-manufacturing process: a conic nozzle deposits rods in an oil bath for further sintering.

were performed on the cross-sectional center of the samples using a Microtest indenter (Nanotest, Micro Materials Ltd. Wrexham, UK) and a Berkovich diamond microindenter. The load was monotonically increased at a rate of 0.1 N/s rate to a maximum load of 2 N and held for 5 s before unloading. The elastic modulus of the ceramic after sintering was finally computed in 48 ± 2 GPa using the Oliver and Pharr method
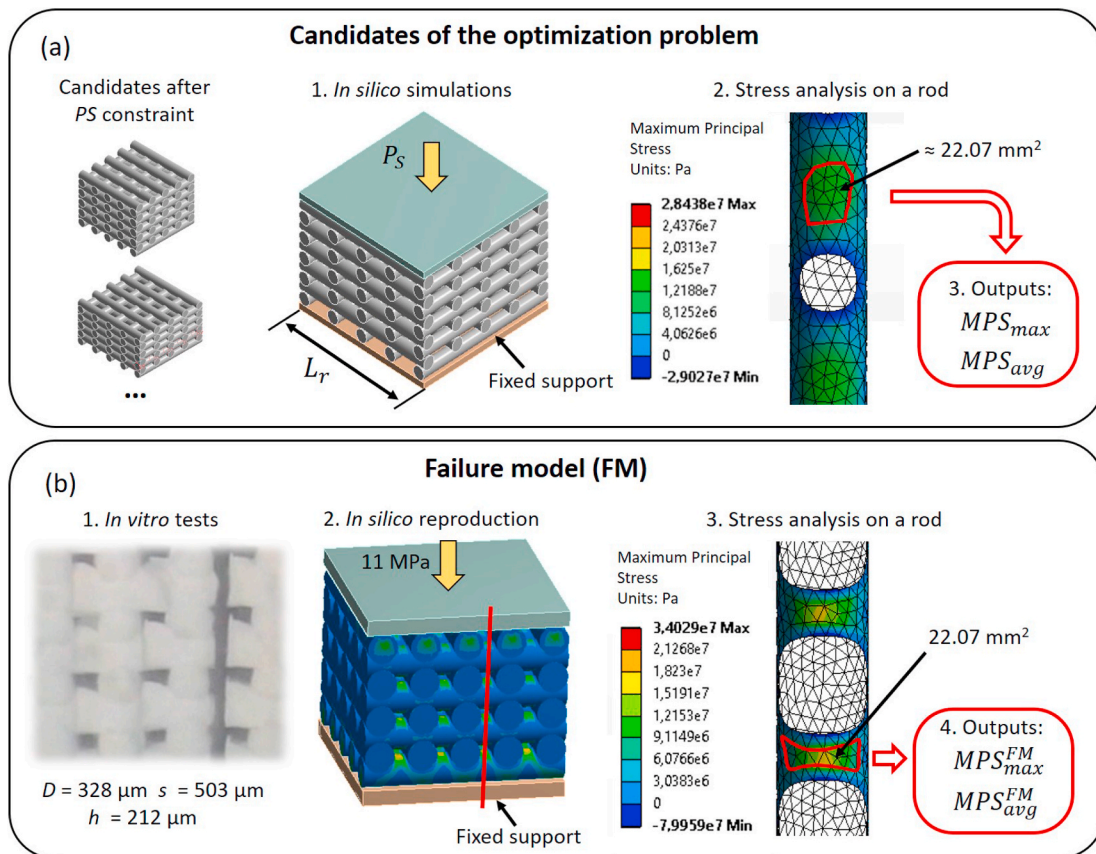

Fig. 2. (a) Procedure to ensure the mechanical integrity of the implant under *in vivo* loads (P_s): (1) example of an *in silico* model of a candidate scaffold cuboid. (2) Distribution of the maximum principal stress (*MPS*) in Pa for the stress analysis. (3) Outputs from each *in silico* model: MPS_{max} and MPS_{avg}. (b) Diagram of the failure model, procedure for selecting of the upper values of MPS_{max} and MPS_{avg}: (1) preliminary *in vitro* compression tests of a scaffold with a specific inner architecture; (2) reproduction of the compression tests by means of an *in silico* model. Red line predicts potential fracture; (3) maximum principal stress analysis on the unsupported surface area between rods. Red perimeter limits the surface area of the unsupported segment between rods considered in the analysis; (4) selection of the MPS_{max}^{FM} and MPS_{avg}^{FM}.

(Oliver and Pharr (1992)).

The controllable geometric variables of the architecture to be optimized, which are inputs of the 3D-printing process, are the diameter of the rods (D), the distance between rods of the same layer (s), and the spacing between contiguous overlapping layers (h), as defined in Fig. 1a. Considering the available conical nozzles (EFD Inc., East Providence, RI, USA) and an average sintering shrinkage of 20%, D can be selected between 264, 328 and 488 μm to avoid clogging problems during the extrusion of ceramic paste. Meanwhile, s is restricted from $1.1 \cdot D$ to $3 \cdot D$ for structural stability reasons during deposition. Finally, h varies between 10 and 42% of D. For each diameter, 100 equally-distributed combinations of s and h were considered to design a total of 300 candidate *in silico* models to perform the optimization algorithm. For computational time savings reasons, the 3D-models were simplified by considering an inner cuboid scaffold cell composed of 5 rods per layer and 10 layers, 5 per orientation (Fig. 2a).

2.2. Optimization problem

Considering both biological and mechanical requirements, the three geometric variables were optimized (D, h, and s) based on the contributions of previous *in vitro*, *in silico*, and *in vivo* TE studies (Hulbert et al. (1970); Story et al. (1998); Lewandrowski et al. (2000); Bohner and Baumgart (2004); Karageorgiou and Kaplan (2005); Miranda et al. (2007); Bai et al. (2010); Murphy and O'Brien (2010); Feng et al. (2011); Amini et al. (2012); Joshi et al. (2013); Roy et al. (2003); Dawson et al. (2018); Zhang et al. (2018); De Wild et al. (2019); Krieghoff et al. (2019); Lanza et al. (2020)). The cost function used in the optimization was related to the biological parameters to guarantee focal adhesion between the cell and the biomaterial, as well as cell proliferation and differentiation: the specific surface area of the cuboid scaffolds (SSA), the porosity of the implants (Φ_S), and the scaffold pore size (PS). Meanwhile, the cost function constraints were mainly referred to the mechanical strength of the HA structures and some limits experienced in the biological parameters, according to:

$$\text{objective function:} \quad max(\Phi_s, SSA, PS)$$
$$\text{constraints:}$$
$$300 \mu m < PS < 700 \ \mu m$$
$$MPS < \textit{failure criteria}$$
\hfill (1)

where MPS is the maximum principal tensile stress of the scaffold subjected to *in vivo* loads.

The porosity Φ_s is extensively proven to improve osteogenesis due to higher cell penetration in numerous *in vivo* applications (Story et al. (1998); Lewandrowski et al. (2000); Roy et al. (2003); Karageorgiou and Kaplan (2005)). This parameter is computed in our potential geometric structures by means of Eq. (2):

$$\Phi_s = \left(1 - \frac{V_s}{V_T}\right) \cdot 100 \tag{2}$$

where V_s is the material volume of the scaffold cell, and V_T is the total volume of the cuboid.

Another key parameter in the structural design is the SSA, which is quantified as:

$$SSA = \frac{A_s}{V_T} \tag{3}$$

where A_s is the surface area of the scaffold pore walls. Modeling the SSA as a bulk volume (m^{-1}) allows playing with the printing variables to optimize the parameter regardless of the manufacturing material. Cell adhesion is based on the specific ligand interactions between cells and their extracellular environment (Murphy and O'Brien (2010)). A larger SSA implies a higher ligand density for cells to develop their spontaneous regeneration mechanisms (Murphy and O'Brien (2010); Lanza

et al. (2020)). Furthermore, previous bioceramic scaffold studies have emphasized its benefits for degradation and protein absorption rates (Bohner and Baumgart (2004); Dawson et al. (2018)), primarily due to the critical role played by its micro-porosity (Zhang et al. (2018)).

The PS plays the double role of cost function and constraint. A minimum PS of 100 μm was historically established for effective cell migration (Hulbert et al. (1970); Karageorgiou and Kaplan (2005)). However, higher cellular infiltration, proliferation, and differentiation rates were obtained with pores greater than 300 μm (Karageorgiou and Kaplan (2005); Amini et al. (2012); Joshi et al. (2013); Krieghoff et al. (2019)). Additionally, large PS is demonstrated to enhance vascularization and mass transport of oxygen (Bai et al. (2010); Feng et al. (2011); Amini et al. (2012); Joshi et al. (2013)). The upper limit of this property is generally determined by the mechanical strength required for the *in vivo* application. However, some studies have reported how a PS greater than 600–700 μm (Feng et al. (2011)) or distance between rods greater than 800 μm (De Wild et al. (2019)) reduces fibrous tissue ingrowth, probably due to its inversely proportional relationship with the SSA (Murphy and O'Brien (2010)). Therefore, upper and lower limits were established based on literature to ensure its optimal effects on regeneration, setting them at 300 and 700 μm, respectively. In our study, PS was defined as the diameter of the potential pore in the longitudinal direction of the metatarsus (Eq. (4)).

$$PS = s - D \tag{4}$$

All the previous parameters were measured in the CAD software Ansys SpaceClaim® (Ansys Inc., Canonsburg, Pennsylvania, U.S.). The second constraint was defined to guarantee the mechanical integrity of the scaffolds during the *in vivo* experiments. The implant will mainly be exposed to compression loads, perpendicular to the printing plane, caused by the proximal bony fragment during the stance phase. A previous study determined that the longitudinal cracking along the load axis direction through the unsupported segment between rods is the predominant failure mode of these scaffolds under compression (Miranda et al. (2007)). Neglecting the influence of starting flaws, the tensile stresses located on the surfaces of these segments are considered responsible for this fracture mode (Miranda et al. (2007)). A failure criteria for the potential structures is numerically defined in subsection 2.4.

2.3. Finite element modeling

Cuboids are widely accepted models for analyzing the mechanical properties of porous biomaterials with repeatability in their lattice structure. Smith et al. (2013) proved that the finite element modeling of a single cell could correctly predict many mechanical yields. Following the same strategy of previous works in the literature (Miranda et al. (2007); Kadkhodapour et al. (2015)), simulations were directly performed on the cuboid models composed of 4x4x5 unit cells. The most unfavorable mechanical condition under ideal contact surfaces was simulated: the one in which the bone-scaffold interface has completely ossified without a tissue bridge through the structure. Two structural steel plates at either end are connected to the implant cuboid (48 GPa of elastic modulus, as reported above) by frictionless contacts. They act as contact surfaces between the scaffold and both proximal and distal bony fragments. While the upper plate applies the pressure that the implant should endure *in vivo* (P_s), the lower one serves as a fixed support. Only displacement in the load application direction is allowed. A diagram for P_s calculation is shown in Fig. 3. Disregarding the mechanical performance of the bone marrow, P_s is estimated by means of Eq. (5):

$$P_s = f_{bone} \cdot \frac{IF}{A_c} \tag{5}$$

where IF is the internal force through the right-back metatarsus of merino sheep during stance phases, A_c is the mean intermediate cortical
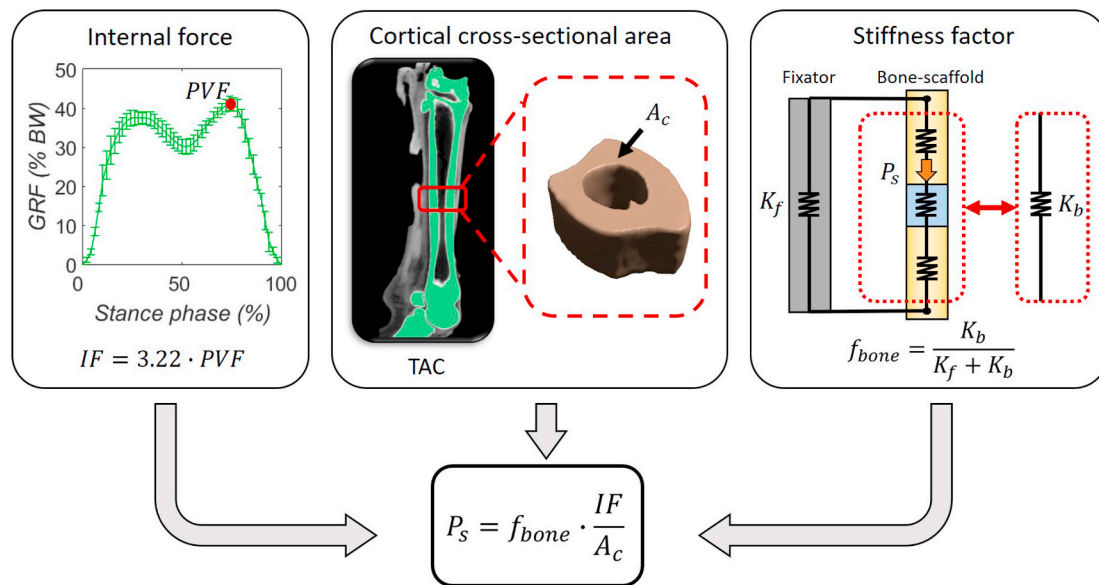
Fig. 3. Scheme of the procedure for estimating the input pressure (P_s) to be applied to scaffolds in the finite element models. The internal force (IF) was calculated from the ground reaction force (GRF) collected by a load platform during gait analysis of healthy animals. The cortical cross-sectional area (A_c) was computed from CT images of sheep metatarsus. The stiffness factor for removing the load through fixator was estimated from a stiffness analysis of the bone-fixator system.

cross-sectional area of the metatarsus, and f_{bone} is a stiffness factor that removes the amount of load through the external fixator. After traversing the operated bone, IF is inverted in unquantifiable muscle activity and ground reaction force GRF (Mora-Macías et al. (2015b); Blázquez-Carmona et al. (2020a,b)). Previous research showed how the GRF reaches a peak vertical force (PVF) in our limb model of 42% of the total body weight (BW) in healthy animals (Mora-Macías et al. (2015b)). In the literature, the IF/PVF ratio was assumed constant to estimate IF (Duda et al. (1997); Mora-Macías et al. (2015a); Blázquez-Carmona et al. (2020a)), and was 3.22 ± 0.46 for the same animal model. This ratio was assumed in TE, estimating an upper limit of forces through the skeletal structure of the limb as:

$$IF = 3.22 \cdot PVF = 3.22 \cdot (0.42 \cdot BW) \tag{6}$$

The mean weight of merino sheep used in previous works was fixed, namely 645.66 ± 29.08 N (Mora-Macías et al. (2015a,b); Blázquez-Carmona et al. (2020a, 2021). Computed tomography images were also taken in a cadaveric right-back limb, which was used in further *in vitro* validation, to evaluate the A_c, quantified as 115.11 mm^2 (Fig. 3). In the meantime, the stiffness factor f_{bone} was obtained by performing a stiffness analysis of the different components among which the IF is distributed. Depending on their stiffnesses, part of the IF goes through the fixation ($K_f = 593$ N/mm) and another part through the bone-scaffold subsystem (K_b). The stiffness of the subsystem K_b was calculated from the length of each component (48.75 mm of each bone fragment and 15 mm of scaffold), their cross-sectional area A_c and their elastic modulus. While an elastic modulus of 21 GPa was considered for the cortical bone tissue according to the nanoindentation study of Mora-Macías et al. (2017), the apparent elastic modulus of each scaffold was previously estimated numerically. Finally, f_{bone} was calculated as:

$$f_{bone} = \frac{K_b}{K_f + K_b} \tag{7}$$

No additional safety factor was applied due to the margin derived from the hypothesis that the animal does not suffer any reduction in the bearing capacity of the operated limb after surgery.

Geometries were imported from the SpaceClaim module to the Static Structural one in Ansys Workbench. The boundary conditions described above were imposed and models were resolved in terms of Maximum Principal Stress (MPS). Nodes, elements and stress values were then exported to Matlab (The MathWorks, Inc., Natick, MA) for further comparison to the stress values obtained in the failure model simulation (section 2.4). The element size varies between models with different D values for computational time-saving reasons without compromising the mesh independence of the MPS.

2.4. Failure criteria

Fig. 2b shows a diagram of the steps followed to set the failure criteria. *In vitro* compression tests were performed on ten 3D-printed cuboid HA scaffolds (3346 × 3346×1494 µm) with a specific architecture (D = 328 µm; s = 503 µm; h = 212.5 µm), giving an experimental macro-scale compressive strength of 11 ± 2 MPa (see Fig. 2b1). This test was numerically reproduced by means of a finite element model (failure model, *FM*) in the same commercial software Ansys Workbench® (Ansys Inc., Canonsburg, Pennsylvania, U.S.), as shown in Fig. 2b2. After the *in silico* application of the pressure corresponding to the experimentally-obtained compressive strength (11 MPa), the failure criteria for the candidate structures was defined according to the maximum stress levels obtained from this *FM* on the surface of the inner unsupported segments between rods (Miranda et al. (2007)): a maximum MPS (MPS_{max}^{FM}) of 16.73 MPa or an average MPS on a fixed surface area (MPS_{avg}^{FM}) of 11.23 MPa (see Fig. 2b3) located on a bottom rod. The surface area to calculate the MPS_{avg} (Fig. 2, red perimeters) was selected in the failure model as the outer faces of the contiguous tetrahedral elements between rods whose superficial nodes presents MPS values in the same magnitude order as the MPS_{max}^{FM}, namely 22.07 mm^2. This surface area was fixed to perform the stress analysis on the simulated candidate cuboid scaffolds. Once the failure stress values was set, each candidate under *in vivo* loads (P_s) was considered to collapse if its maximum MPS (MPS_{max}) or an average MPS (MPS_{avg}) on the fixed surface area of an unsupported segment (22.07 mm^2) exceeds the values obtained in the FM (MPS_{max}^{FM} and MPS_{avg}^{FM}), as shown in Fig. 2a. The defined failure criteria was focused on the rod surface faces due to the higher stresses achieved in bending. In the line of the area-weighted mean stress calculated in the finite element simulations of Rainer et al. (2012), all the MPS_{avg} mentioned above were calculated as:

$$MPS_{avg} = \frac{\sum_i MPS_i \cdot w_i}{\sum_i w_i} \qquad (8)$$

where MPS_i is the solved maximum principal stress for the ith element, w_i is the outer surface area, and $\sum_i w_i$ is the total surface area fixed in the *FM*, being around 22.07 mm^2.

Only the candidates which met the *PS* constraint were considered for this mechanical analysis for computational time-saving reasons. The resulting MPS_{max} and MPS_{avg} point clouds were fitted as surfaces for further analysis of the contribution of each geometric variable. As a first approach, a polynomial surface of degree 2 in *h* and degree 2 in *s* was used, normalized by *D*. The fitting and determination coefficients (R^2 and *p* values) will be detailed in the results section.

Finally, the force at which the selected structure would collapse *in silico* ($F_{failure}$) was calculated for further *in vitro* validation of the failure criteria. This force can be estimated from the *IF*, which was applied to our *in silico* models by means of P_s, increased by the factor MPS_{max}^{FM}/MPS_{max} or MPS_{avg}^{FM}/MPS_{avg}. These factors correspond to the necessary increase in P_s for the optimal cuboid to reach the MPS_{max}^{FM} or the MPS_{avg}^{FM}, respectively.

$$F_{failure} = IF \cdot \min\left(\frac{MPS_{max}^{FM}}{MPS_{max}}, \frac{MPS_{avg}^{FM}}{MPS_{avg}}\right) \qquad (9)$$

2.5. Experimental characterization and validation

The geometrical parameters (the porosity Φ_s, the *SSA*, and the *PS*) of the further selected architecture were characterized *in vitro* and validated with respect to the CAD design values, following the steps shown in Fig. 4. Six HA patient-specific scaffolds were manufactured by robocasting following the procedure described in previous subsections. Their outer shapes were designed from tomographic images taken from a cadaveric sheep metatarsus. X-ray microtomographic images of all specimens were also taken and analyzed using a COUGAR tomography (Y.COUGAR SMT®, Yxlon, Hudson, OH, USA) and the commercial software AVIZO® (Thermo Fisher Scientific, Waltham, MA, USA) to calculate the parameters to be validated of an inner CT cuboid.

Finally, the manufactured scaffolds were mechanically tested *in vitro* to validate the consistency of the defined failure criteria under the *in silico* boundary conditions: the proper effect of equivalent stiffness or the failure criteria based on the stresses on the inter-rod segment surfaces. The strength of the optimized 3D-printed implants to the metatarsal internal forces was characterized by simulating the *in vivo* mechanical environment considered in the numerical model (Fig. 5a). The external

fixator was assembled in the cadaveric sheep metatarsus. Two osteotomies were subsequently performed using an oscillating saw, resulting in a 15 mm removable bony fragment between the distal and proximal frames of the fixator. Each scaffold was inserted into the induced gap and fixed in the bone-scaffold contact surfaces with rigid polyurethane-based resin to avoid stress concentration. This resin also plays the role of ossified bone tissue between the scaffold and cortical bone surfaces. Compression tests, from a preload of −100 N until breakage, were performed on the scaffold-fixator system using a push-pull testing machine MTS 858 MINIBIONIX II® (MTS System Corporation, Eden Prairie, MN, USA). The compressive strength of the scaffold was compared with the force calculated *in silico* to force non-compliance with the failure criteria ($F_{failure}$).

3. Results

3.1. Selection of the geometric architecture

Extensive analyses were carried out to understand the effects of each geometric parameter evaluated in the optimization problem. Fig. 6 shows the distribution of the objective function and constraints for each diameter *D* as a function of the other geometrical variables: *s* and *h* normalized by *D*. Starting with the Φ_s (Fig. 6a), the *s* parameter to a lesser extent and the *h* to a greater extent raise the porosity of the structure equivalently for all *D*, reaching a maximum value of 68.35% for the highest spacing dimensions controlled by both *s* and *h* variables. Concerning *SSA* (Fig. 6b), both *s* and *h* parameters significantly influence this objective function, giving maximum values for low and high *s/D* and *h/D* rates, respectively. However, the rod diameter *D* has a more significant influence on *SSA*, inducing increases between 903 and 2868 m^{-1} among consecutive printing nozzles. In relation to the *PS* (Fig. 6c), *D* and *s* variables control the pore size in the longitudinal direction, which increases with the *s/D* rate until values between 528 and 976 μm. Only 150 structures met the *PS* constraint and were numerically simulated to verify the mechanical feasibility. Finally, Fig. 6d and e show the change in the maximum principal stress (MPS_{max} and MPS_{avg}, respectively) as a point cloud and a fitting polynomial surface per rod diameter. Their fitting coefficients and R-square and p-values determination coefficients are shown in Table 1. Both parameters evaluated on the unsupported segments depend mainly on the *s* variable due to the bending forces introduced by the shear force on the inter-rod contacts.

To compare the candidate structures after imposing the defined constraints, *SSA* and *PS* were normalized by maximum reference values, SSA_{max} and PS_{max}. The reference value for *SSA* was defined by the
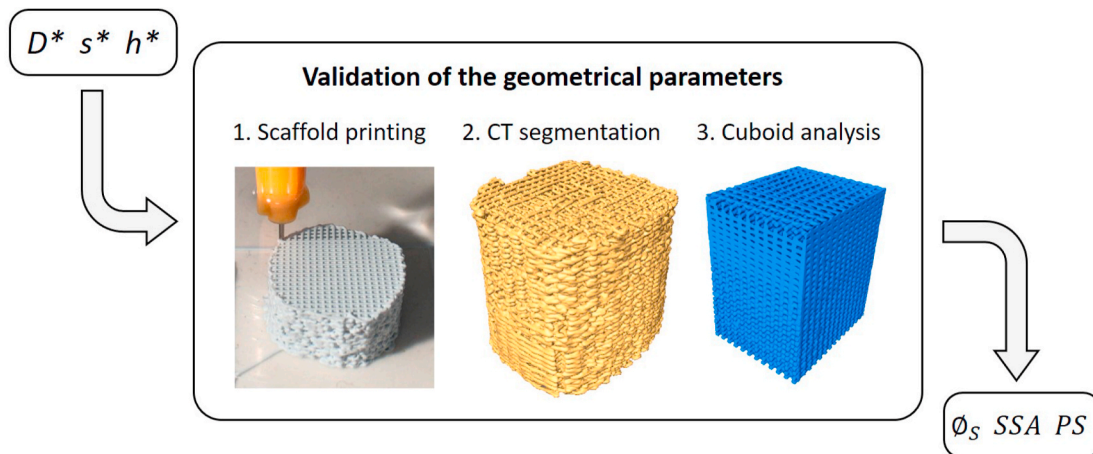

Fig. 4. Diagram of the procedure for validating the *in vitro* geometrical parameters (porosity Φ_s, the *SSA*, and the *PS*) with respect to the CAD design values considered in the optimization problem: (1) patient-specific scaffolds printing with the selected architecture; (2) tomographic imaging and CT segmentation; (4) selection of an inner CT cuboid to perform the calculations.
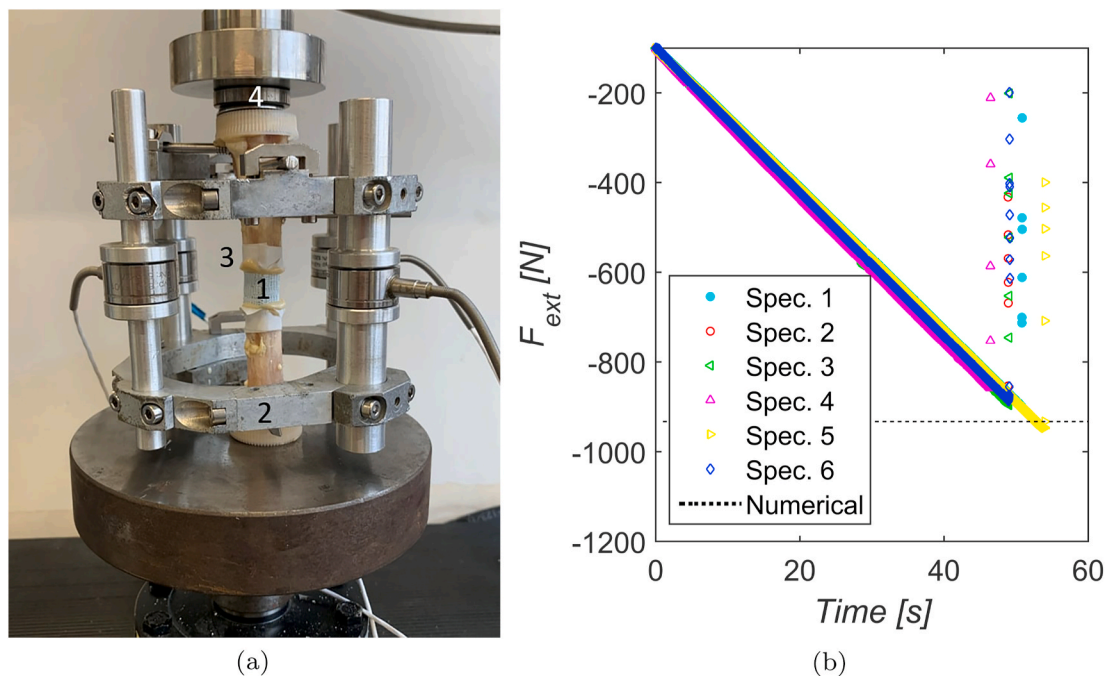
(a)

(b)

Fig. 5. (a) Scaffold-fixator system in a cadaveric sheep metatarsus during the characterization and calibration: (1) patient-specific HA scaffold; (2) external fixator; (3) rigid polyurethane-based resin on the scaffold-bone contact surface; (4) ball joint. (b) Compression tests on the fixator-scaffold system implanted on a cadaveric sheep metatarsus from a −100 N preload to collapse of the ceramic scaffold. Each scaffold is represented by a different marker (specimen 1 to 6). The compressive strength in N according to the *in silico* model ($F_{failure}$) is also included (dotted black line).

maximum specific surface area of *n* non-interconnected rods (curved surfaces and plane ends) which assemble the structure:

$$SSA_{max} = \max\left(\frac{n\cdot\left(\pi\cdot D\cdot L_r + 2\cdot\pi\cdot\left(\frac{D}{2}\right)^2\right)}{n\cdot\pi\cdot\left(\frac{D}{2}\right)^2\cdot L_r}\right) = 15695.23 \ m^{-1} \quad (10)$$

where L_r is the length of the rods which compose the simplified cuboid scaffolds.

Similarly, the reference value for the *PS* was defined by the maximum value within the geometrical limitations, which corresponds to the greater distance between rods extruded by the larger nozzle:

$$PS_{max} = \max(s - D) = \max(3D - D) = 976 \ \mu m \quad (11)$$

Fig. 6f shows the 16 candidate scaffolds that overcame all optimization problem constraints, as well as their values for each normalized objective function. Assuming the same weight for all objective functions, the compromised architecture, calculated as the maximum Euclidean norm, is defined by the following geometric values: 264 μm of *D*, 625 μm of *s*, and 228 μm of *h*. The objective functions of the optimization problem take the following values in the selected scaffold: $\Phi_s = 59.30\%$, $SSA = 5768.91 \ m^{-1}$, and $PS = 360.80 \ \mu$m.

3.2. Experimental characterization results

The results from the characterization of the six 3D-printed scaffolds by means of the tomographic images are presented in Table 2. Design values are also included as a reference. While the measured Φ_s was 62.94 ± 1.49%, an error of 6.14% to the design value, the experimental *SSA* was quantified as 5288.07 ± 448.18 m^{-1} and 8.32% of error. The lowest error in reference to the numerical values was obtained for the *PS* (363.73 ± 20.65 μm), which was 1.04%.

Regarding the calibration of the failure criteria, the MPS_{max} and MPS_{avg} values in the *in silico* simulation of the selected structure were 12.03 and 10.51 MPa, respectively. Therefore, the force at which the

optimized scaffold would collapse in accordance with its numerical model ($F_{failure}$) was computed as 932.09 N. The compression tests performed on the 3D-printed structures with the metatarsal bony fragments stabilized by the external fixator are displayed together with $F_{failure}$ in Fig. 5b. The implants collapsed at compressive load levels of 895.10 ± 25.55 N, an error of 3.97% with respect to the numerical prediction.

4. Discussion

A procedure for the structural optimization of ceramic scaffolds for critical-sized load-bearing defects was described, considering both biological and mechanical aspects derived from the implantation of flexible fixations for stabilize the defect. The optimization problem converged on the following design geometrical parameters: $\Phi_s = 59.30\%$, $SSA = 5768.91 \ m^{-1}$, and $PS = 360.80 \ \mu$m. Overall these values are in line with previous successful *in vivo* studies in long-bony models (Wang et al. (2010); Cipitria et al. (2013); Pobloth et al. (2018)). Wang et al. (2010) achieved high ossification on a goat tibiae 30 mm defect employing internal fixation and ceramic scaffolds with 70% porosity and 450 μm of *PS* after 24 post-surgical weeks. Pobloth et al. (2018) also reached a considerable bone volume and mineral content through a 30 mm defect in sheep tibiae using ceramic-polymer composite scaffolds with a porosity level of 60%, characterized by interconnected macro-pores with *PS* of 100–500 μm. Although porosity values are not detailed, the scaffolding architectural pattern used by Cipitria et al. (2013) in tibia sheep presents similarities with the one optimized in this paper. Vidal et al. (2020) inserted 3D-printed calcium phosphate scaffolds into a 35 mm long sheep metatarsus defect, managing to bridge it three months after surgery. The geometrical parameters of their structure were quite different from those optimized in this work: 489.7 μm of *PS* and 81.03% of total porosity. Nevertheless, a plate screwed to the bone was used to stabilize the defect, which would greatly reduce the mechanical constraints of the problem. Vidal et al. (2020) also quantified the *SSA* in 22.1 m^2/g. Although their methods are not explicitly mentioned, other authors quantified this physicochemical property in the same units through the adsorption of gas molecules on the solid surface using BET
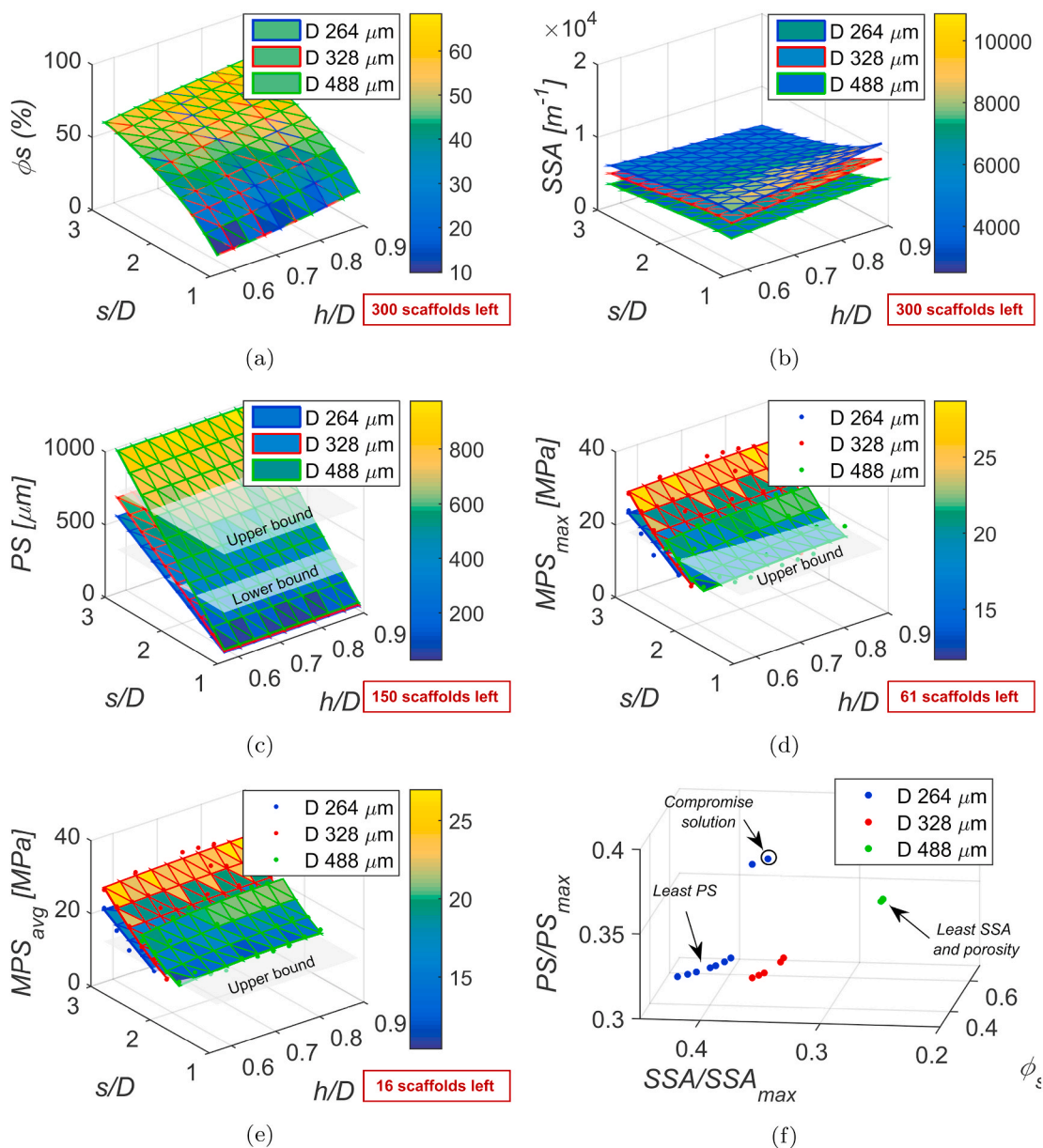
Fig. 6. Surface evolution of the parameters analyzed in the structural optimization problem as a function of the geometric variables, *s* (x-axis), *h* (y-axis) and *D* (264 μm, blue surface; 328 μm, red surface; 488 μm, green surface): (a) porosity, Φ_s %; (b) specific surface area, *SSA*; (c) pore size, *PS*; (d) maximum *MPS*; (e) average *MPS* in the unsupported segment between rods; (f) analysis of the geometric structures that satisfy the constraints of the optimization problem. Objective functions, *PS* (z-axis) and *SSA* (x-axis), were normalized by maximum reference values. The number of candidate scaffolds that overcomes each constraint are specified (red dialog boxes).

Table 1
Coefficient of two-degree polynomial fitting of the MPS_{max} and MPS_{avg} results of the candidate scaffolds' computational analysis as a function of the geometrical parameters *D*, *s*, and *h*. Also specified are the fitting goodness coefficients: R^2 and p-value.

$$XX(D, h, s) = p00 + p10 \cdot \frac{h}{D} + p01 \cdot \frac{s}{D} + p20 \cdot \left(\frac{h}{D}\right)^2 + p11 \cdot \frac{h \cdot s}{D} + p02 \cdot \left(\frac{s}{D}\right)^2$$

XX	D	p00	p01	p01	p20	p11	p02	R^2	$p - value$
MPS_{max}	264	−20.07	−10.21	21.08	−0.74	3.69	−2.38	0.80	< 0.01
	326	6.75	10.17	−8.66	−5.52	0.18	4.75	0.95	< 0.01
	488	30.53	33.75	−40.95	−17.49	−0.57	13.14	0.84	< 0.01
MPS_{avg}	264	−8.26	−1.96	7.97	−2.19	1.80	0.33	0.82	< 0.01
	326	4.06	10.46	−7.32	−7.07	1.08	4.25	0.96	< 0.01
	488	4.11	39.55	−18.78	−28.02	4.04	7.14	0.91	< 0.01

Table 2
CAD design values and measures of the geometric parameters evaluated on the six 3D-printed scaffolds through the tomographic images: porosity Φ_s, specific surface area (*SSA*), and pore size (*PS*). Mean and standard deviation between specimens are also detailed.

Scaffold	Φ_s(%)	$SSA\ [m^{-1}]$	$PS\ [\mu m]$
Design values	59.30	5768.91	360.80
1	63.92	5027.73	344.21
2	64.43	6103.89	363.01
3	63.65	4999.40	353.20
4	63.43	4941.31	365.02
5	61.57	5507.21	403.09
6	60.63	5148.84	354.12
Mean and std	62.94 ± 1.49	5288.07 ± 448.18	363.73 ± 20.65

(Brunauer-Emmett-Teller) technology (Cholas et al. (2016); Uchino et al. (2010)). Since *SSA* is a scale-dependent property, results obtained by this method are not directly comparable with our imaging measurements (Hanaor et al. (2014)). Most previous works agree on using hollow cylinders to introduce supplied products that accelerate the biological process, including recombinant bone morphogenetic proteins, autologous cancellous bone graft, or vascular plugs (Cipitria et al. (2013); Pobloth et al. (2018); Vidal et al. (2020)). This design would be compatible with the proposed optimization problem using the volume corresponding to the bone marrow as the hollow channel since only the cortical cross-sectional area was considered in the P_S calculation. Furthermore, other works reported the influence of drying and sintering temperature on the morphology and size of the residual micro-porosity (Martínez-Vázquez et al. (2017)). Despite its proven influence on osteogenesis (Karageorgiou and Kaplan (2005)), those manufacturing conditions that enhance the compressive strength were selected in this macro-scale optimization process due to the critical mechanical constraints of this clinical problem.

After manufacturing six specimens by robocasting, the comparison between the geometric design parameters (Φ_s, *SSA*, *PS*) and those calculated *in vitro* revealed a slight deviation (Table 2). These findings tie well with previous studies in different materials and manufacturing processes (Lee et al. (2006); Wilson et al. (2011)). Lee et al. (2006) obtained a disparity of results in polymeric scaffolds with orthogonal cubic lattice structure manufactured by injection molding depending on the *PS* and *%* closed pores. For a 300 μm of *PS*, errors between 27.41 and 63.21% were quantified *in vitro* for different levels of CAD porosity with

respect to the apparent porosity (Lee et al. (2006)). Nevertheless, no significant errors were reported for higher *PS*, 600 and 900 μm. This effect was attributed to the high impacts of manufacturing defects on low pore sizes. A more similar pattern of porosity discrepancies was reported by Wilson et al. (2011) on scaffolds produced by casting ceramic materials into square cross-sectional molds. The lowest difference in porosity between HA specimens was reported at higher sintering temperatures due to more significant densification, namely 15.90% for 1250 °C. In the same way, defects related to the manufacturing process are the primary source of deviation between design Φ_s and the CAD values in our structures, from the ink deposition to the hardly controllable shrinkage by sintering. For instance, Fig. 7a illustrates tomographic images of some localized gaps caused by air bubbles during the printing. In spite of its exclusion from the imaging analysis through the inner cuboid selection, the contoured volume of patient-specific scaffolds reduces the overall porosity of the structure, as show in Fig. 7b. These manufacturing error source can be extrapolated to the other validated parameters, *SSA* and *PS*. Despite the divergence, these parameters' values are still consistent with those implemented in previous experimental works (Wang et al. (2010); Cipitria et al. (2013); Pobloth et al. (2018)).

In all structures, the maximum principal stresses of each rod layer after applying loads appeared on the unsupported inter-rod segments. This conclusion agrees with the numerical and experimental study of Miranda et al. (2007) on HA scaffolds fabricated by robocasting. Miranda et al. (2007) relate this effect to an accumulation of tensile stress along the rod axes. As previously reported, the *MPS* surfaces (Fig. 6e and f) show a great influence of the variable *s*, which seems to indicate a great impact of the bending in the segment. In addition, the greatest stresses are located on the top, or bottom, rods. This result is also in agreement with the fracture of the bottom rods before the inner structural cracks reported by *in situ* tests of Miranda et al. (2007). Regarding the experimental validation, the compressive strength of our specimens occurred at similar load levels (895.10 ± 29.55 N) to those predicted *in silico* (932.09 N). Therefore, all hypothesis used in numerical models seem to be reasonable, including the simplification of the stress analysis to the surface elements on the unsupported inter-rod segments. Moreover, in line with the experimental scaffolding studies of Giannitelli et al. (2014b) and Uth et al. (2017), an indirect relationship was observed between porosity and a compressive modulus. Thus, a slight increase in porosity relative to the design value (Table 2) is reflected in a slightly lower resistance to compression loads (Fig. 5b).
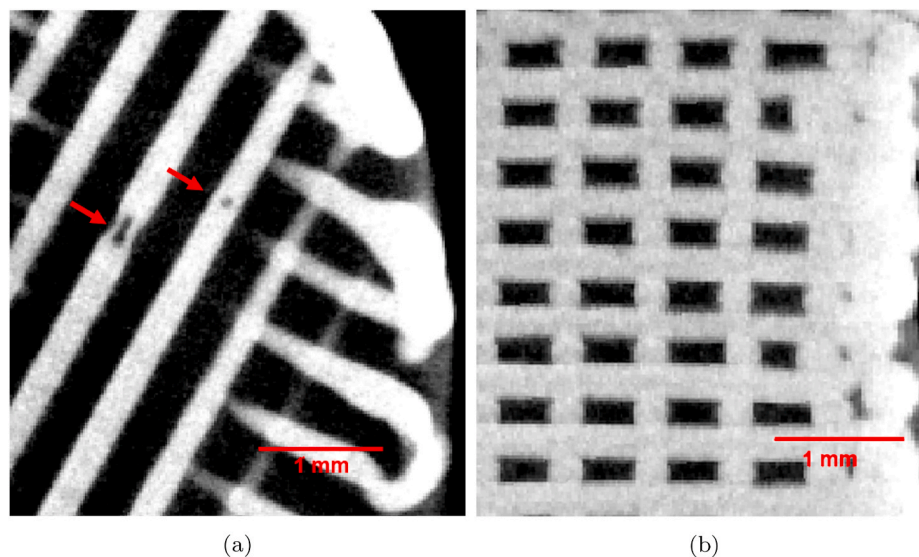

(a)   (b)

Fig. 7. Tomographic images of internal structural defects in the HA scaffolds derived from the manufacturing process: (b) gaps caused by internal bubbles in the nuzzle during printing (red arrows); (a) less porous contour and heterogeneity in the rod spacing.

There are some limitations to this study. First of all, the simplification of the mechanical problem *in vivo* to compressive axial loads, neglecting the bending moments which would appear in our bony model during stance phases. Secondly, the manufacturing technology used generally introduces defects that slightly reduce the optimized parameters, as previously discussed. Also, Mora-Macías et al. (2017) reported a trabecular structure in woven bone during consolidation under similar external fixation. Thus, a non-regular structural pattern could benefit the biological proliferation of the defect. By cons, Lee et al. (2018) proved how the orthogonal lattice enhances the compressive strength and modulus of the structure. Consequently, greater mechanical constraints, supported by an alternative *FM*, would be required to guarantee the applicability of this methodology to not regularly oriented structures. The scaffolds for this application will only have the aforementioned manufacturing defects (Fig. 7) as an additional incentive to osteogenesis. Despite exceeding objectives of the current work, these optimization strategies together with multiscale approaches (Sanz-Herrera et al. (2008, 2009; 2010)) could allow the mechanical characterization of the optimized structure for alternative numerical applications, such as a flow rate optimization (Nguyen et al. (2018)) or a data-driven mechanical tissue characterization at different scales (Mora-Macías et al. (2020); Sanz-Herrera et al. (2021)).

As for the reproducibility of the presented study, given that the optimization problem considers specific data related to the external fixator and bony model, procedures with alternatives fixations and animal models are subject to previous gait analysis and a study of the *in vivo* internal forces. Agostinho et al. (2012) and Mora-Macías et al. (2015b) reported greater ground reaction forces (*% BW*) in ovine forelimbs, which would imply more limiting mechanical restrictions in the failure criteria. To exemplify the dissimilarities with other animal models, axial forces in rabbit tibia (*% BW*) exceeded the forces in ovine long-bones and bending moments (*% BW*) seem to be more significant, according to the *in vivo* study of Reifenrath et al. (2012). Regarding its applicability to other clinical problems with distribution of tissue material properties (e.g. metastatic lesions or bone-device integration problems), Falcinelli et al. (2019) and Molinari et al. (2021) opted for defining stress criterion based on the local ash density. This parameter was in turn estimated by the Hounsfield Unit distribution of CT-images according to Yosibash et al. (2010). The numerical-experimental strategy proposed in the current work could be applied through cadaveric samples of the tissue and numerical models based on CT images. In addition, since the *MPS*, *PS* and Φ_s seem to be mainly controlled by the *s* parameter, it seems reasonable to build advanced constitutive models for bone tissues based on the trabecular geometry (e.g. Tb.Th, Tb.Sp or BV/TV). They should also be supported by experimental validations or numerical comparisons from micro-CT images to ensure a proper mathematical mimic of the real mechanical behavior. Lastly, recent evidence of material property inconsistency at different length scales (Schwiedrzik et al. (2017); Casari et al. (2019)) makes future analysis interesting in terms of scaffold components.

In conclusion, an easily reproducible numerical model was defined *in silico* and experimentally validated to optimize ceramic scaffolds for long-bony defects stabilized by external fixations. For a particular bony model, hind limb sheep metatarsus, the optimized levels of porosity and pore size are comparable with previous successful *in vivo* works. Despite the greater mechanical constraints derived from its relative flexibility, the inclusion of external fixation in the bone tissue engineering models opens the door to future research, such as tissue comparisons with defects externally stabilized, instrumentation and force analysis *in vivo*, or comparisons under a self-mechanical environment with works based on distraction osteogenesis, in which external fixations are widely used.

Author statement

Pablo Blázquez-Carmona: Finite Element simulations, Experimental validation, Writing- Original draft preparation, Writing-Reviewing and Editing. **José Antonio Sanz-Herrera**: Conceptualization, Methodology, Writing- Reviewing and Editing. **Francisco Javier Martínez-Vázquez**: Manufacture of specimens, Writing- Reviewing and Editing. **Jaime Domínguez**: Supervision. **Esther Reina-Romo**: Conceptualization, Methodology, Supervision, Writing- Reviewing and Editing.

Declaration of competing interest

The authors declare that they have no known competing financial interests or personal relationships that could have appeared to influence the work reported in this paper.

Acknowledgments

Appendix A. Supplementary material

Table A.3
Summary of the parameters used in the optimization problem and its validation.

Parameter	Equation	Value	Description
,Variables which define the geometric architecture of the scaffolds			
D	–	264, 328 or 488 μm	Diameter of the rods
s	–	$\in[1.1D, 3D]$	Distance between rods of the same layer
h	–	$\in[0.1D, 0.42D]$	Layer spacing
Geometrical data of the cuboid scaffolds for the calculations in the optimization problem			
V_s	From CAD	$f(D, s, h)$	Interconnected rod volume
V_T	From CAD	$f(D, s, h)$	Total volume
A_s	From CAD	$f(D, s, h)$	Surface area of the interconnected rods
L_r	From CAD	$f(D, s, h)$	Length of the rods of the cuboid scaffold
Parameters of the optimization problem			
Φ_s	$\Phi_s = \left(1 - \dfrac{V_s}{V_T}\right) \cdot 100$	$f(D, s, h)$	Porosity of the cuboids
SSA	$\dfrac{A_s}{V_T}$	$f(D, s, h)$	Specific surface area of the cuboids
PS	$s - D$	$f(D, s, h)$	Pore size of the cuboids
MPS_{max}	After simulation	$f(D, s, h)$	*MPS* on the segment between rods

(*continued on next page*)

Table A.3 (*continued*)

Parameter	Equation	Value	Description
MPS_{avg}	After simulation	f(D, s, h)	Mean MPS on the segment between rods
Specific data of our bony model and scaffold material			
BW	From previous works	645.66 ± 29.08 N	Mean body weight of a sheep
IF	$3.22 \cdot (0.42 \cdot BW)$	873.19 N	Internal force through a sheep metatarsus
A_c	From TAC images	115.11 mm^2	Cortical cross-sectional area of a metatarsus
Parameters of the numerical simulations and the failure model FM			
K_f	Measured	593 ± 21 N/mm	Stiffness of the external fixator
f_{bone}	$\dfrac{K_b}{K_f + K_b}$	f(D, s, h)	Stiffness factor
P_s	$f_{bone} \cdot \dfrac{IF}{A_c}$	f(D, s, h)	Pressure to be supported by the scaffold
MPS_{max}^{FM}	After simulation of the FM	16.73 MPa	MPS for collapse
MPS_{avg}^{FM}	After simulation of the FM	11.23 MPa	Average MPS for collapse
Parameters of the in vitro validation			
$V_{T,CT}$	From micro-CT	2555.08 ± 53.96 mm^3	Total volume of the 3D-printed scaffolds
$F_{failure}$	$A_c \cdot P_s \cdot \min\left(\dfrac{MPS_{max}^{FM}}{MPS_{max}}, \dfrac{MPS_{avg}^{FM}}{MPS_{avg}}\right)$	932.09 N	Force at which the selected scaffold would collapse
Maximum reference values of PS and SSA parameters for normalization			
SSA_{max}	$\max\left(\dfrac{n \cdot \left(\pi \cdot D \cdot L_r + 2 \cdot \pi \cdot \left(\frac{D}{2}\right)^2\right)}{n \cdot \pi \cdot \left(\frac{D}{2}\right)^2 \cdot L_r}\right)$	15695.23 m^{-1}	Maximum SSA between candidates
PS_{max}	$\max(s - D)$	976 μm	Maximum *Greatest PS* between candidates

References

Agostinho, F.S., Rahal, S.C., Araújo, F.A., Conceição, R.T., Hussni, C.A., El-Warrak, A.O., Monteiro, F.O., 2012. Gait analysis in clinically healthy sheep from three different age groups using a pressure-sensitive walkway. BMC Vet. Res. 8, 87.

Amini, A.R., Laurencin, C.T., Nukavarapu, S.P., 2012. Bone tissue engineering: recent advances and challenges. Crit. Rev. Biomed. Eng. 40.

Bai, F., Wang, Z., Lu, J., Liu, J., Chen, G., Lv, R., Wang, J., Lin, K., Zhang, J., Huang, X., 2010. The correlation between the internal structure and vascularization of controllable porous bioceramic materials in vivo: a quantitative study. Tissue Eng. 16, 3791–3803.

Berthiaume, F., Maguire, T.J., Yarmush, M.L., 2011. Tissue engineering and regenerative medicine: history, progress, and challenges. Annu. Rev. Chem. Biomol. Eng 2, 403–430.

Blázquez-Carmona, P., Mora-Macías, J., Morgaz, J., Fernández-Sarmiento, J.A., Domínguez, J., Reina-Romo, E., 2020a. Mechanobiology of bone consolidation during distraction osteogenesis: bone lengthening vs. bone transport. Ann. Biomed. Eng. 1–13.

Blázquez-Carmona, P., Sanchez-Raya, M., Mora-Macías, J., Gómez-Galán, J.A., Domínguez, J., Reina-Romo, E., 2020b. Real-time wireless platform for in vivo monitoring of bone regeneration. Sensors 20, 4591.

Blázquez-Carmona, P., Mora-Macías, J., Sanz-Herrera, J.A., Morgaz, J., Navarrete-Calvo, R., Domínguez, J., Reina-Romo, E., 2021. Mechanical influence of surrounding soft tissue on bone regeneration processes: a bone lengthening study. Ann. Biomed. Eng. 49, 642–652.

Boccaccio, A., Uva, A.E., Fiorentino, M., Lamberti, L., Monno, G., 2016a. A mechanobiology-based algorithm to optimize the microstructure geometry of bone tissue scaffolds. Int. J. Biol. Sci. 12, 1.

Boccaccio, A., Uva, A.E., Fiorentino, M., Mori, G., Monno, G., 2016b. Geometry design optimization of functionally graded scaffolds for bone tissue engineering: a mechanobiological approach. PloS One 11, e0146935.

Bohner, M., 2000. Calcium orthophosphates in medicine: from ceramics to calcium phosphate cements. Injury 31, D37–D47.

Bohner, M., Baumgart, F., 2004. Theoretical model to determine the effects of geometrical factors on the resorption of calcium phosphate bone substitutes. Biomaterials 25, 3569–3582.

Bressan, E., Favero, V., Gardin, C., Ferroni, L., Iacobellis, L., Favero, L., Vindigni, V., Berengo, M., Sivolella, S., Zavan, B., 2011. Biopolymers for hard and soft engineered tissues: application in odontoiatric and plastic surgery field. Polymers 3, 509–526.

Casari, D., Pethö, L., Schürch, P., Maeder, X., Philippe, L., Michler, J., Zysset, P., Schwiedrzik, J., 2019. A self-aligning microtensile setup: application to single-crystal gaas microscale tension–compression asymmetry. J. Mater. Res. 34, 2517–2534.

Chocholata, P., Kulda, V., Babuska, V., 2019. Fabrication of scaffolds for bone-tissue regeneration. Materials 12, 568.

Cholas, R., Padmanabhan, S.K., Gervaso, F., Udayan, G., Monaco, G., Sannino, A., Licciulli, A., 2016. Scaffolds for bone regeneration made of hydroxyapatite microspheres in a collagen matrix. Mater. Sci. Eng. C 63, 499–505.

Cipitria, A., Reichert, J.C., Epari, D.R., Saifzadeh, S., Berner, A., Schell, H., Mehta, M., Schuetz, M.A., Duda, G.N., Hutmacher, D.W., 2013. Polycaprolactone scaffold and reduced rhbmp-7 dose for the regeneration of critical-sized defects in sheep tibiae. Biomaterials 34, 9960–9968.

Dawson, E.R., Suzuki, R.K., Samano, M.A., Murphy, M.B., 2018. Increased internal porosity and surface area of hydroxyapatite accelerates healing and compensates for low bone marrow mesenchymal stem cell concentrations in critically-sized bone defects. Appl. Sci. 8, 1366.

De Wild, M., Ghayor, C., Zimmermann, S., Rüegg, J., Nicholls, F., Schuler, F., Chen, T.H., Weber, F.E., 2019. Osteoconductive lattice microarchitecture for optimized bone regeneration. 3D Print. Addit. Manuf. 6, 40–49.

den Boer, F.C., Patka, P., Bakker, F.C., Wippermann, B.W., van Lingen, A., Vink, G.Q., Boshuizen, K., Haarman, H.J.T.M., 1999. New segmental long bone defect model in sheep: quantitative analysis of healing with dual energy x-ray absorptiometry. J. Orthop. Res. 17, 654–660.

Dias, M.R., Guedes, J.M., Flanagan, C.L., Hollister, S.J., Fernandes, P.R., 2014. Optimization of scaffold design for bone tissue engineering: a computational and experimental study. Med. Eng. Phys. 36, 448–457.

Duda, G.N., Eckert-Hübner, K., Sokiranski, R., Kreutner, A., Miller, R., Claes, L., 1997. Analysis of inter-fragmentary movement as a function of musculoskeletal loading conditions in sheep. J. Biomech. 31, 201–210.

El-Rashidy, A.A., Roether, J.A., Harhaus, L., Kneser, U., Boccaccini, A.R., 2017. Regenerating bone with bioactive glass scaffolds: a review of in vivo studies in bone defect models. Acta Biomater. 62, 1–28.

Eqtesadi, S., Motealleh, A., Pajares, A., Miranda, P., 2015. Effect of milling media on processing and performance of 13-93 bioactive glass scaffolds fabricated by robocasting. Ceram. Int. 41, 1379–1389.

Falcinelli, C., Di Martino, A., Gizzi, A., Vairo, G., Denaro, V., 2019. Mechanical behavior of metastatic femurs through patient-specific computational models accounting for bone-metastasis interaction. J. Mech.Behav.Biomed. Mater. 93, 9–22.

Feng, B., Jinkang, Z., Zhen, W., Jianxi, L., Jiang, C., Jian, L., Guolin, M., Xin, D., 2011. The effect of pore size on tissue ingrowth and neovascularization in porous bioceramics of controlled architecture in vivo. Biomed. Mater. 6, 015007.

Giannitelli, S.M., Accoto, D., Trombetta, M., Rainer, A., 2014a. Current trends in the design of scaffolds for computer-aided tissue engineering. Acta Biomater. 10, 580–594.

Giannitelli, S.M., Rainer, A., Accoto, D., De Porcellinis, S., De-Juan-Pardo, E.M., Guglielmelli, E., Trombetta, M., 2014b. Optimization approaches for the design of additively manufactured scaffolds. In: Tissue Engineering. Springer, pp. 113–128.

Giannitelli, S., Mozetic, P., Trombetta, M., Rainer, A., 2015. Combined additive manufacturing approaches in tissue engineering. Acta Biomater. 24, 1–11.

Gomes, P., Fernandes, M., 2011. Rodent models in bone-related research: the relevance of calvarial defects in the assessment of bone regeneration strategies. Lab. Anim 45, 14–24.

Gugala, Z., Lindsey, R.W., Gogolewski, S., 2007. New approaches in the treatment of critical-size segmental defects in long bones. In: Macromolecular Symposia. Wiley Online Library, pp. 147–161.

Hanaor, D.A., Ghadiri, M., Chrzanowski, W., Gan, Y., 2014. Scalable surface area characterization by electrokinetic analysis of complex anion adsorption. Langmuir 30, 15143–15152.

Histing, T., Menger, M.D., Pohlemann, T., Matthys, R., Fritz, T., Garcia, P., Klein, M., 2016. An intramedullary locking nail for standardized fixation of femur osteotomies to analyze normal and defective bone healing in mice. JoVE, e54472.

Hollister, S.J., Maddox, R., Taboas, J.M., 2002. Optimal design and fabrication of scaffolds to mimic tissue properties and satisfy biological constraints. Biomaterials 23, 4095–4103.

Hulbert, S., Young, F., Mathews, R., Klawitter, J., Talbert, C., Stelling, F., 1970. Potential of ceramic materials as permanently implantable skeletal prostheses. J. Biomed. Mater. Res. 4, 433–456.

Joshi, V.S., Lei, N.Y., Walthers, C.M., Wu, B., Dunn, J.C., 2013. Macroporosity enhances vascularization of electrospun scaffolds. J. Surg. Res. 183, 18–26.

Kadkhodapour, J., Montazerian, H., Darabi, A.C., Anaraki, A., Ahmadi, S., Zadpoor, A., Schmauder, S., 2015. Failure mechanisms of additively manufactured porous biomaterials: effects of porosity and type of unit cell. J. Mech.Behav.Biomed. Mater. 50, 180–191.

Karageorgiou, V., Kaplan, D., 2005. Porosity of 3d biomaterial scaffolds and osteogenesis. Biomaterials 26, 5474–5491.

Krieghoff, J., Picke, A.K., Salbach-Hirsch, J., Rother, S., Heinemann, C., Bernhardt, R., Kascholke, C., Möller, S., Rauner, M., Schnabelrauch, M., et al., 2019. Increased pore size of scaffolds improves coating efficiency with sulfated hyaluronan and mineralization capacity of osteoblasts. Biomater. Res. 23, 26.

Lanza, R., Langer, R., Vacanti, J.P., Atala, A., 2020. Principles of Tissue Engineering. Academic press.

Lao, J., Lacroix, J., Nohra, J., Naaman, N., Sautier, J.M., Jallot, E., 2014. Chemical imaging of the reconstruction of new bone and trace elements inside bioactive glass scaffolds in vivo: a multimodal and quantitative micro-ion beam analysis. Surf. Interface Anal. 46, 702–706.

Lee, K.W., Wang, S., Lu, L., Jabbari, E., Currier, B.L., Yaszemski, M.J., 2006. Fabrication and characterization of poly (propylene fumarate) scaffolds with controlled pore structures using 3-dimensional printing and injection molding. Tissue Eng. 12, 2801–2811.

Lee, J.B., Maeng, W.Y., Koh, Y.H., Kim, H.E., 2018. Porous calcium phosphate ceramic scaffolds with tailored pore orientations and mechanical properties using lithography-based ceramic 3d printing technique. Materials 11, 1711.

Lewandrowski, K.U., Gresser, J.D., Bondre, S.P., Silva, A.E., Wise, D.L., Trantolo, D.J., 2000. Developing porosity of poly (propylene glycol-co-fumaric acid) bone graft substitutes and the effect on osteointegration: a preliminary histology study in rats. J. Biomater. Sci. Polym. Ed. 11, 879–889.

Li, Y., Chen, S.K., Li, L., Qin, L., Wang, X.L., Lai, Y.X., 2015. Bone defect animal models for testing efficacy of bone substitute biomaterials. J.Orthop.Translat. 3, 95–104.

Liu, X., Li, X., Fan, Y., Zhang, G., Li, D., Dong, W., Sha, Z., Yu, X., Feng, Q., Cui, F., et al., 2010. Repairing goat tibia segmental bone defect using scaffold cultured with mesenchymal stem cells. J. Biomed. Mater. Res. B Appl. Biomater. 94, 44–52.

Martínez-Vázquez, F., Pajares, A., Miranda, P., 2017. Effect of the drying process on the compressive strength and cell proliferation of hydroxyapatite-derived scaffolds. Int. J. Appl. Ceram. Technol. 14, 1101–1106.

Mauney, J.R., Jaquiéry, C., Volloch, V., Heberer, M., Martin, I., Kaplan, D.L., 2005. In vitro and in vivo evaluation of differentially demineralized cancellous bone scaffolds combined with human bone marrow stromal cells for tissue engineering. Biomaterials 26, 3173–3185.

McGovern, J.A., Griffin, M., Hutmacher, D.W., 2018. Animal models for bone tissue engineering and modelling disease. Disease models & mechanisms 11.

Miranda, P., Pajares, A., Saiz, E., Tomsia, A.P., Guiberteau, F., 2007. Fracture modes under uniaxial compression in hydroxyapatite scaffolds fabricated by robocasting. J. Biomed. Mater. Res. Part A: An Off J Soc Biomater, Japanese Soc Biomater, Australian Soc Biomater Korean Soc Biomater 83, 646–655.

Miranda, P., Pajares, A., Saiz, E., Tomsia, A.P., Guiberteau, F., 2008. Mechanical properties of calcium phosphate scaffolds fabricated by robocasting. J. Biomed. Mater. Res. Part A: An Off J Soc Biomater, Japanese Soc Biomater, Australian Soc Biomater Korean Soc Biomater 85, 218–227.

Molinari, L., Falcinelli, C., Gizzi, A., Di Martino, A., 2021. Effect of pedicle screw angles on the fracture risk of the human vertebra: a patient-specific computational model. J. Mech. Behav.Biomed. Mater. 116, 104359.

Mora-Macías, J., Reina-Romo, E., López-Pliego, M., Giráldez-Sánchez, M., Domínguez, J., 2015a. In vivo mechanical characterization of the distraction callus during bone consolidation. Ann. Biomed. Eng. 43, 2663–2674.

Mora-Macías, J., Reina-Romo, E., Morgaz, J., Domínguez, J., 2015b. In vivo gait analysis during bone transport. Ann. Biomed. Eng. 43, 2090–2100.

Mora-Macías, J., Pajares, A., Miranda, P., Domínguez, J., Reina-Romo, E., 2017. Mechanical characterization via nanoindentation of the woven bone developed during bone transport. J. Mech.Behav.Biomed. Mater. 74, 236–244.

Mora-Macías, J., Ayensa-Jiménez, J., Reina-Romo, E., Doweidar, M.H., Domínguez, J., Doblaré, M., Sanz-Herrera, J.A., 2020. A multiscale data-driven approach for bone tissue biomechanics. Comput. Methods Appl. Mech. Eng. 368, 113136.

Murphy, C.M., O'Brien, F.J., 2010. Understanding the effect of mean pore size on cell activity in collagen-glycosaminoglycan scaffolds. Cell Adhes. Migrat. 4, 377–381.

Nguyen, T., Carpentier, O., Monchau, F., Chai, F., Hornez, J.C., Hivart, P., 2018. Numerical optimization of cell colonization modelling inside scaffold for perfusion bioreactor: a multiscale model. Med. Eng. Phys. 57, 40–50.

Oh, D.Y., Choi, J.Y., Kim, K.J., Park, J.H., Cho, D.W., Rhie, J.W., 2015. Development of an advanced external fixation device for rat femur defect. Tissue Eng. Regen. Med 12, 154–161.

Oliver, W.C., Pharr, G.M., 1992. An improved technique for determining hardness and elastic modulus using load and displacement sensing indentation experiments. J. Mater. Res. 7, 1564–1583.

Pina, S., Ribeiro, V.P., Marques, C.F., Maia, F.R., Silva, T.H., Reis, R.L., Oliveira, J.M., 2019. Scaffolding strategies for tissue engineering and regenerative medicine applications. Materials 12, 1824.

Pobloth, A.M., Schell, H., Petersen, A., Beierlein, K., Kleber, C., Schmidt-Bleek, K., Duda, G.N., 2018. Tubular open-porous β-tricalcium phosphate polycaprolactone scaffolds as guiding structure for segmental bone defect regeneration in a novel sheep model. J. Tissue Eng.Regen. Med 12, 897–911.

Rainer, A., Moroni, L., Computer-aided Tissue Engineering .

Rainer, A., Giannitelli, S.M., Accoto, D., De Porcellinis, S., Guglielmelli, E., Trombetta, M., 2012. Load-adaptive scaffold architecturing: a bioinspired approach to the design of porous additively manufactured scaffolds with optimized mechanical properties. Ann. Biomed. Eng. 40, 966–975.

Reifenrath, J., Gottschalk, D., Angrisani, N., Besdo, S., Meyer-Lindenberg, A., 2012. Axial forces and bending moments in the loaded rabbit tibia in vivo. Acta Vet. Scand. 54, 21.

Roy, T.D., Simon, J.L., Ricci, J.L., Rekow, E.D., Thompson, V.P., Parsons, J.R., 2003. Performance of degradable composite bone repair products made via three-dimensional fabrication techniques. J. Biomed. Mater. Res. Part A: An Official Journal of The Society for Biomaterials, The Japanese Society for Biomaterials, and The Australian Society for Biomaterials and the Korean Society for Biomaterials 66, 283–291.

Sachlos, E., Czernuszka, J., et al., 2003. Making tissue engineering scaffolds work. review: the application of solid freeform fabrication technology to the production of tissue engineering scaffolds. Eur. Cell. Mater. 5, 39–40.

Sanz-Herrera, J., García-Aznar, J., Doblaré, M., 2008. Micro–macro numerical modelling of bone regeneration in tissue engineering. Comput. Methods Appl. Mech. Eng. 197, 3092–3107.

Sanz-Herrera, J., García-Aznar, J., Doblaré, M., 2009. On scaffold designing for bone regeneration: a computational multiscale approach. Acta Biomater. 5, 219–229.

Sanz-Herrera, J., Doblaré, M., García-Aznar, J., 2010. Scaffold microarchitecture determines internal bone directional growth structure: a numerical study. J. Biomech. 43, 2480–2486.

Sanz-Herrera, J.A., Mora-Macías, J., Ayensa-Jiménez, J., Reina-Romo, E., Doweidar, M. H., Domínguez, J., Doblaré, M., 2021. Data-driven computational simulation in bone mechanics. Ann. Biomed. Eng. 49, 407–419.

Schwiedrzik, J., Taylor, A., Casari, D., Wolfram, U., Zysset, P., Michler, J., 2017. Nanoscale deformation mechanisms and yield properties of hydrated bone extracellular matrix. Acta Biomater. 60, 302–314.

Seal, B., Otero, T., Panitch, A., 2001. Polymeric biomaterials for tissue and organ regeneration. Mater. Sci. Eng. R Rep. 34, 147–230.

Silber, J.S., Anderson, D.G., Daffner, S.D., Brislin, B.T., Leland, J.M., Hilibrand, A.S., Vaccaro, A.R., Albert, T.J., 2003. Donor site morbidity after anterior iliac crest bone harvest for single-level anterior cervical discectomy and fusion. Spine 28, 134–139.

Smith, M., Guan, Z., Cantwell, W., 2013. Finite element modelling of the compressive response of lattice structures manufactured using the selective laser melting technique. Int. J. Mech. Sci. 67, 28–41.

Story, B.J., Wagner, W.R., Gaisser, D.M., Cook, S.D., Rust-Dawicki, A.M., 1998. In vivo performance of a modified csti dental implant coating. Int. J. Oral Maxillofac. Implants 13.

Uchino, T., Yamaguchi, K., Suzuki, I., Kamitakahara, M., Otsuka, M., Ohtsuki, C., 2010. Hydroxyapatite formation on porous ceramics of alpha-tricalcium phosphate in a simulated body fluid. J. Mater. Sci. Mater. Med. 21, 1921–1926.

Uth, N., Mueller, J., Smucker, B., Yousefi, A.M., 2017. Validation of scaffold design optimization in bone tissue engineering: finite element modeling versus designed experiments. Biofabrication 9, 015023.

Vidal, L., Kampleitner, C., Krissian, S., Brennan, M.Á., Hoffmann, O., Raymond, Y., Maazouz, Y., Ginebra, M.P., Rosset, P., Layrolle, P., 2020. Regeneration of segmental defects in metatarsus of sheep with vascularized and customized 3d-printed calcium phosphate scaffolds. Sci. Rep. 10, 1–11.

Wang, C., Wang, Z., Li, A., Bai, F., Lu, J., Xu, S., Li, D., 2010. Repair of segmental bone-defect of goat's tibia using a dynamic perfusion culture tissue engineering bone. J. Biomed. Mater. Res. Part A: An Official Journal of The Society for Biomaterials, The Japanese Society for Biomaterials, and The Australian Society for Biomaterials and the Korean Society for Biomaterials 92, 1145–1153.

Wilson, C., Van Blitterswijk, C., Verbout, A., Dhert, W., de Bruijn, J.D., 2011. Scaffolds with a standardized macro-architecture fabricated from several calcium phosphate ceramics using an indirect rapid prototyping technique. J. Mater. Sci. Mater. Med. 22, 97–105.

Yang, S., Leong, K.F., Du, Z., Chua, C.K., 2002. The design of scaffolds for use in tissue engineering. part ii. rapid prototyping techniques. Tissue Eng. 8, 1–11.

Yosibash, Z., Tal, D., Trabelsi, N., 2010. Predicting the yield of the proximal femur using high-order finite-element analysis with inhomogeneous orthotropic material properties. Phil. Trans. Math. Phys. Eng. Sci. 368, 2707–2723.

Zhang, K., Fan, Y., Dunne, N., Li, X., 2018. Effect of microporosity on scaffolds for bone tissue engineering. Regenerative biomaterials 5, 115–124.